Energy & Environmental Science

Accepted Manuscript

ROYAL SOCIETY OF CHEMISTRY

www.rsc.org/ees

Unique 3D Heterojunction Photoanode Design to Harness Charge Transfer for Efficient and Stable Photoelectrochemical Water Splitting

Jungang Hou,[ab*] Huijie Cheng,[a] Osamu Takeda,[b] Hongmin Zhu[ab*]

[a]School of Metallurgical and Ecological Engineering, University of Science and Technology Beijing, Beijing 100083, China

[b]Tohoku University, 6-6-02 Aramaki-Aza-Aoba, Aoba-ku, Sendai, 980-8579 Japan

Corresponding author: jhou@ustb.edu.cn; hzhu@material.tohoku.ac.jp

Abstract:

Photoelectrochemical (PEC) solar water splitting over oxynitrides is a promising process for renewable hydrogen production. However, the oxynitride heterojunction photoanodes with high charge-separation efficiency and stability, which have unique dimensionality-dependent integrative and synergic effects are intriguing but still underdeveloped. Here, we design and fabricate the 1D/2D nanorod/nanosheet-assembled tantalum oxynitride (TaON) photoanode with the high PEC activity. Especially, an integrated 3D heterojunction photoanodes comprising the 1D/2D barium-doped TaON (Ba-TaON) array and 2D carbon nitride (C_3N_4) nanosheets decorated with CoO_x nanoparticles as a novel stack design were firstly prepared and the 3D CoO_x/C_3N_4/Ba-TaON photoanodes with the remarkable photostability reached the pronounced photocurrent of 4.57 mA/cm^2 at 1.23 V vs. RHE under AM 1.5G simulated sunlight. More broadly, the harness charge transfer process of this unique 3D heterojunction photoanodes with the intrinsic requirements, has

been identified by the quantitative analysis combined with the electrochemical impedance and photoluminescence analysis. All the results highlight the great significance of the 3D dimensionality-dependent heterojunction as a promising photoelectrode model for the application in solar conversion. The cooperating amplification effects of nanoengineering from composition regulation, morphology innovation and heterojunction construction provide a valuable insight for the creating more purpose-designed (oxy)nitride photoelectrodes with highly efficient performance.

KEYWORDS: Three-dimensional; TaON; heterojunction; photoanode; solar water splitting

1. Introduction

Developing artificial photosynthesis routes using solar energy is an attractive scientific and technological goal to address the increasing global demand for energy and to reduce the impact on climate change from energy production.[1] Solar energy collection, conversion and storage are three key processes for practical applications and these processes can all be integrated in a single monolithic photoelectrochemical (PEC) water splitting cell. PEC water splitting offers the capability of harvesting the energy in solar radiation and transferring it directly to chemical bonds for easy storage, transport, and use in the form of hydrogen.[2-3] Since TiO_2-based photoelectrochemical cell was used to split water into hydrogen and oxygen by Fujishima and Honda in 1972, most metal oxides as photoelectrodes, such as TiO_2,[4] WO_3,[5] Fe_2O_3,[6] $BiVO_4$,[7] and $SrTiO_3$[8] have received immense attention for the enhancement of the PEC performance. However, different (oxy)nitrides,[9,10] such as TaON,[11-15] Ta_3N_5,[16-18] $SrNbO_2N$,[19] and $LaTiO_2N$,[20] have also been found to be visible light responsive photocatalysts for water splitting. Especially, tantalum (oxy)nitride with the suitable band gap and band position, is considered as a promising photoanode for solar water splitting. However, the serious recombination of the photogenerated charges are definitely detrimental to the PEC performance of these (oxy)nitride photoanodes. Thus, it is essential to guide the design of the (oxy)nitride photoelectrodes through controlling recombination process.

It is well-known that nanostructured engineering could be employed to improve the solar-driven PEC performance.[21,22] Especially, various dimensional heterostructures, such as zero-dimensional (0D) quantum dots,[23] one-dimensional (1D) nanowires,[24] two-dimensional (2D) layered quantum wells,[25] epitaxial nanosheet-nanowire heterostructures,[26] and three-dimensional (3D) nanowire networks,[27] are nevertheless very interesting due to its potential to open up new opportunities, which is ascribed to these architectures that provide an appealing platform with well-defined

structures and interfaces, offering long optical paths for efficient light absorption, high quality conducting channels for rapid electron-hole separation and charge transport, as well as high surface areas for fast interfacial charge transfer and electrochemical reactions.[23-28] Especially, existing efforts have overwhelmingly focused on different dimensional tantalum based (oxy)nitride photoanodes. For example, polycrystalline Ta_3N_5 or TaON nanotube arrays on the Ta substrate were prepared by anodization of tantalum foil.[29,30] Ta_3N_5 nanorod arrays were produced via a through-mask anodization method and a subsequent nitridation process using anodic alumina as the mask and relative high voltage.[31] Moreover, TaON is a promising candidate for both photocatalytic and PEC water splitting.[10-14] Although there have been some reports of the fabrication of nanotructured TaON photoanodes, to the best of our knowledge, there is no any report about dimensionality-dependent oxynitride photoanode.

For the efficient seperation of photogenerated electrons and holes, the heterojunction engineering is a prospective solution about TaON, such as CdS@TaON,[32] Ag/AgCl/TaON,[33] C_3N_4/TaON,[34] $CaFe_2O_4$/TaON,[35] and carbon-Cu_2O/TaON,[36] have shown excellent photocatalytic and PEC activity. Recently, graphitic C_3N_4 with medium band gap as well as thermal and chemical stability in ambient environment, possesses the performance of H_2 or O_2 production from water splitting.[37] For examples, the g-C_3N_4/$CuInS_2$ heterostructure gives rise to a stable photocurrent generation, becasue g-C_3N_4 has beneficial effects on charge carrier kinetics, leading to a +0.15 V shift on onset potential compared to that of the bare $CuInS_2$ photocathode.[38] 3D WO_3/C_3N_4 heterojunctions decorated with CoO_x nanoparticles exhibited significantly enhanced PEC water oxidation performance, including a large photocurrent density and high stability.[39] Therefore, an three-dimensional heterojunction oxynitride photoanodes would be a great strategy for further improving the efficiency of solar energy conversion.

The practical application of oxynitride photoelectrodes is seriously hindered by poor photostability. To resolve this problem, the surface modification due to the surface barriers and defects could be conducted through improving interfacial charge-transfer and water-oxidation kinetics.[40] For instance, highly dispersed CoO_x nanoparticles on the TaON photoanode efficiently scavenge photogenerated holes and effectively suppress self-oxidative deactivation of the TaON surface, resulting in a stable photocurrent.[13] The porous TaON film electrode prepared on conducting glass showed significantly high quantum efficiency, after loading of $IrO_2 \cdot nH_2O$ nanoparticles as a cocatalyst for water oxidation.[41] Therefore, the appropriate water oxidation catalyst (WOC) modified the heterojunction oxynitride photoanode is equally important as it improves the PEC efficiency.

Here, we design and fabricate the first 1D/2D nanorod/nanosheet-assembled TaON photoanode by a controllable vapor-phase hydrothermal technique and subsequent nitridation. To overcome the intrinsically poor charge transport properties and serious stability, the critical advance is the use of an integrated 3D heterojunction photoanodes comprising the 1D/2D barium-doped TaON array and 2D C_3N_4 nanosheets decorated with CoO_x nanoparticles as an innovative stack design, thereby achieving the pronounced photocurrent of 4.57 mA/cm^2 at 1.23 V vs. RHE under AM 1.5G simulated sunlight. This enhancement originates primarily from effective charge migration according to the analysis of PEC performance, the quantitative analysis combined with the electrochemical impedance and photoluminescence analysis. In this regard, the synergistic effects of nanoengineering from composition regulation, morphology innovation and heterojunction construction show great significance of designing highly efficient and dimensionality-dependent photoelectrodes for the application in solar conversion.

2. Experimental Section

2.1 Fabrication of TaON and Ba-TaON arrays

A Ta foil with a thickness of 0.25 mm (Alfa Aesar) was washed in ethanol, acetone, isopropanol and deionized water each for 60 minutes before used. The clean Ta foil was suspended in HF aqueous solution with the different concentration (M1 = 0.15 M; M2 = 0.20 M; M3 = 0.25 M; M4 = 0.50 M) in a Teflon-lined autoclave, which was then heated at 180~240 ^{o}C for 0~6 h to grow F-containing Ta_2O_5 (F-Ta_2O_5) arrays on the Ta foil. The Ba precursor was introduced by dipping the F-Ta_2O_5 arrays into an aqueous solutuion of 0.1 M $Ba(NO_3)_2$ for ~10 s and dried with a N_2 gun according to the previous work.[41] After heat-treatment, the resultant F-Ta_2O_5 arrays with and without Ba on the Ta foil under a gaseous atmosphere of NH_3 with a flow of 20 mL min^{-1} and heated at 650~750 °C for 3~10 h, transformed into the formation of nanostructured TaON and Ba-TaON arrays.

2.2 Fabrication of CoO_x/C_3N_4/Ba-TaON heterojunction arrays

First, bulk C_3N_4 was synthesized by directly heating low-cost melamine based on the previous work.[42] Then, 20 mg of bulk C_3N_4 was dispersed in 100 mL isopropyl alcohol at room temperature and exfoliated by ultrasonication for 12 h. After centrifugation, the exfoliated C_3N_4 nanosheets was collected by pipette. Secondly, the nanostructured Ba-TaON array was immersed into 0.1 mg/mL C_3N_4 nanosheets dispersions for 1 h and then dried in a nitrogen stream. After repeating this process for three times, the resulting sample was transferred to a furnace and annealed at 350 ^{o}C for 1 h in N_2 atmosphere with a ramp rate of 2 ^{o}C/min to improve the adhesion between C_3N_4 nanosheet and Ba-TaON array for the formation of C_3N_4/Ba-TaON heterojunction arrays. Finally, 1 mM of $Co(CH_3COO)_2{\cdot}4H_2O$ was dissolved in 25.0 mL of ethanol, followed by addition of 0.35~0.40 mL of 25% ammonium hydroxide under vigorous stirring. After stirring for 10 min, the solution with the C_3N_4/Ba-TaON photoanode was transferred into an autoclave. The autoclave was sealed and maintained at 393 K for 1 h. After naturally cooled to room temperature, the electrodes were

thoroughly washed with deionized water and dried in air.

2.3 Characterization

The obtained products were characterized with powder X-ray diffraction (XRD, MAC Science Co. Ltd Japan) using Cu K_α (λ = 0.1546 nm) and XRD patterns were obtained for 10-90^o 2θ by step scanning with a step size of 0.02^o. The morphology and size of the resultant powders were characterized by a Zeiss Ultra 55 field-emission scanning electron microscope (SEM) associated with X-ray energy-dispersive spectrometer (EDX). Transmission electron microscope (TEM) images were captured on the transmission electron microscopy (TEM, JEM-2010) at an acceleration voltage of 200 kV. The chemical states of the sample were determined by X-ray photoelectron spectroscopy (XPS) in a VG Multilab 2009 system with a monochromatic Al K_α source and charge neutralizer. The optical properties of the samples were analyzed by UV-vis diffuse reflectance spectroscopy (UV-vis DRS) using a UV-vis spectrophotometer (UV-2550, Shimadzu).

2.4 Photoelectrochemical Water Splitting

The photoelectrochemical water splitting was carried out in a three-electrode system, as shown in scheme S1, where the Ba-TaON, C_3N_4/Ba-TaON and CoO_x/C_3N_4/Ba-TaON photoanodes (the irradiation area was 1 cm^2), a Ag/AgCl electrode and a high surface area platinum mesh act as working electrode, reference electrode and counter electrode, respectively. An aqueous solution of 1.0 M NaOH was used as the electrolyte (pH = 13.6). The electrolyte was stirred and purged with Ar gas before the measurements. The photoelectrodes were illuminated with AM 1.5G simulated sunlight (100 mW/cm^2) from a commercial solar simulator. According to the Nernst equation (E_{RHE} = $E_{Ag/AgCl}$ + 0.059pH + 0.197), where E_{RHE} was the potential vs. a reversible hydrogen potential, $E_{Ag/AgCl}$ was the potential vs. Ag/AgCl electrode, and pH was the pH value of electrolyte. The wavelength dependent the incident photon to current efficiency was calculated according to the

following equation:

$$IPCE(\%) = \frac{1240 \times i_{ph}}{\lambda \times p_{in}} \times 100$$

where i_{ph} is the photocurrent (mA), λ is the wavelength (nm) of incident radiation, and p_{in} is the incident light irradiance on the semiconductor electrode at the selected wavelength (mW).[43] Photocurrent–potential curves were measured at a rate of 30 mV/s. The wavelength dependence of IPCE was measured under monochromatic irradiation from a Xe lamp equipped with bandpass filters (central wavelengths: 400, 420, 440, 460, 480, 500, 520 and 540 nm).

The hydrogen and oxygen evolution by photoelectrochemical water splitting was conducted in the air-tight reactor connected to a closed gas circulation system. The various photoanodes were biased at 1.0 V vs. RHE in a stirred aqueous solution of 1.0 M NaOH (pH = 13.6) under AM 1.5G simulated sunlight. The amount of hydrogen or oxygen was determined by a gas chromatography (GC–3240, TCD, Ar carrier). For Faradaic efficiency, a two-electrode cell (no reference electrode) was used to measure the Faradaic efficiency. The CoO_x/C_3N_4/Ba-TaON photoanode and a Pt foil were used as a working electrode and a counter electrode, respectively. The bias was 1.0 V. The area of the CoO_x/C_3N_4/Ba-TaON photoanode was about 1 cm^2. The cell was sealed and was purged by Ar for half an hour and no O_2 or N_2 was detected before the Faradaic efficiency measurement.

3. RESULTS AND DISCUSSION

3.1 Morphological and Structural Characterization.

The realization of this tentative design needs feasible and straightforward procedures. The schematic illustration for the fabrication process of hierarchical tantalum-based array is presented in Figure 1. Firstly, fluorine-containing hierarchical Ta_2O_5 (F-Ta_2O_5) array directly grew on the Ta substrate, was prepared by an in-situ hydrothermal treatment process with the controllable

concentration of HF solution. Then, the Ba precursor was introduced by dipping the F-Ta_2O_5 arrays into an aqueous $Ba(NO_3)_2$ solution. Moreover, the unique nanosheet/nanorod- assembled Ba-TaON array were obtained after subsequent nitridation route with appropriate temperature. Finally, with the 3D Ba-TaON array, the construction of the heterojunction comprising layered C_3N_4 semiconductors on the array was conducted by the heat-treatment. Then, the CoO_x nanoparticles modified the C_3N_4/Ba-TaON heterojunction photoanode were achieved by the further hydrothermal process. Herein, Figure 1 unambiguously depicts the sketch of the three dimentional multilayered CoO_x/C_3N_4/Ba-TaON heterojunction photoanode.

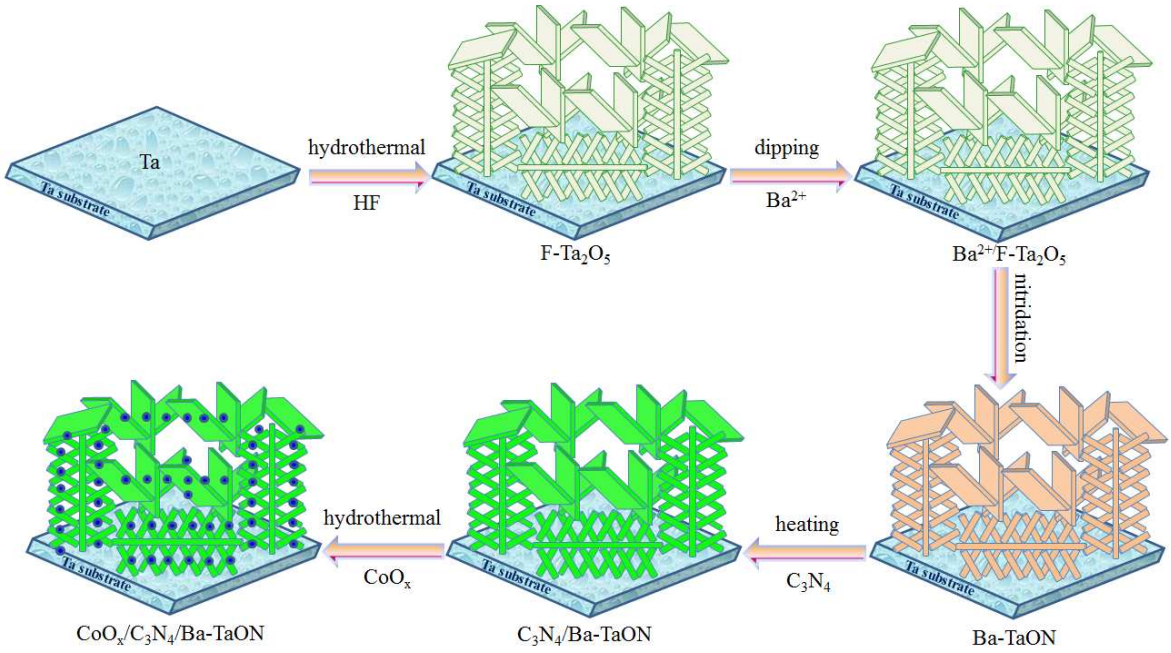

Figure 1. Schematic sketch of three-dimensional CoO_x/C_3N_4/Ba-TaON heterojunction arrays.

To understand the formation of the shape-dependent F-Ta_2O_5 and TaON arrays, the concentration-dependent morphology evolution was recorded. The schematic sketch and the relative TEM images of shape-dependent F-Ta_2O_5 and TaON arrays by the increasing concentration of HF solution (M1 < M2 < M3 < M4) were shown (Figure 2 and Figure S2~S7). Under the relative low concentration of HF, the morphology has been showed for the F-Ta_2O_5 nanorod array (Figure 2a) by

the vapor-phase hydrothermal process in the mild HF environmental condition.[18,36] Increasing a little amount of HF (M2) with the relative high vapor pressure, a small quantity of F-Ta_2O_5 nanosheets appeared on the surface of the F-Ta_2O_5 nanorod array (Figure 2d). Especially, parts of 1D nanorod and 2D nanosheet were intercrossed each other. As shown in Figure 2g, under the use of HF solution (M3), the homogeneous 1D/2D nanorod/nanosheet-assembled architectures were achieved because it is sufficient to dissolve the Ta substrate by this HF concentration in the reaction zone. Particularly, the multilayered photoanode with the nanosheet-like flowers (top layer) and nanorod-assembled caterpillars (underlayer) as the stack integration were formed on the surface of Ta substrate. Soaring to the highest concentration of HF solution (M4), the spindle-like F-Ta_2O_5 nanostructures were uniformly produced, as shown in Figure 2j. Currently, it is noted that the white F-Ta_2O_5 thin film framents were observed in the autoclave after the vapor-phase hydrothermal reaction, indicating the initial F-Ta_2O_5 film was peeled off the Ta substrate and then the spindle-like F-Ta_2O_5 array was grown again on the Ta substrate due to the high HF vapor pressure. Moreover, the dimensionality-dependent TaON arrays were fabricated by the subsequent nitridation using the F-Ta_2O_5 arrays as raw materials. In order to convince the difference of various-dimensional F-Ta_2O_5 and TaON array, the magnified SEM images were presented in Figure 2behk. Especially, the large-scale 1D/2D nanorod/nanosheet-assembled TaON array including a large amount of nanosheets with side length of *ca.* 1~3 μm and 98.2% of exposed {001} faceted surfaces and most of nanorod-assembled caterpillars, has been observed (Figure S5 and S7). Thus, the comparison of the shape-dependent F-Ta_2O_5 and TaON arrays indicates that there is no obvious change upon the morphology before and after nitridation for the various photoanodes.

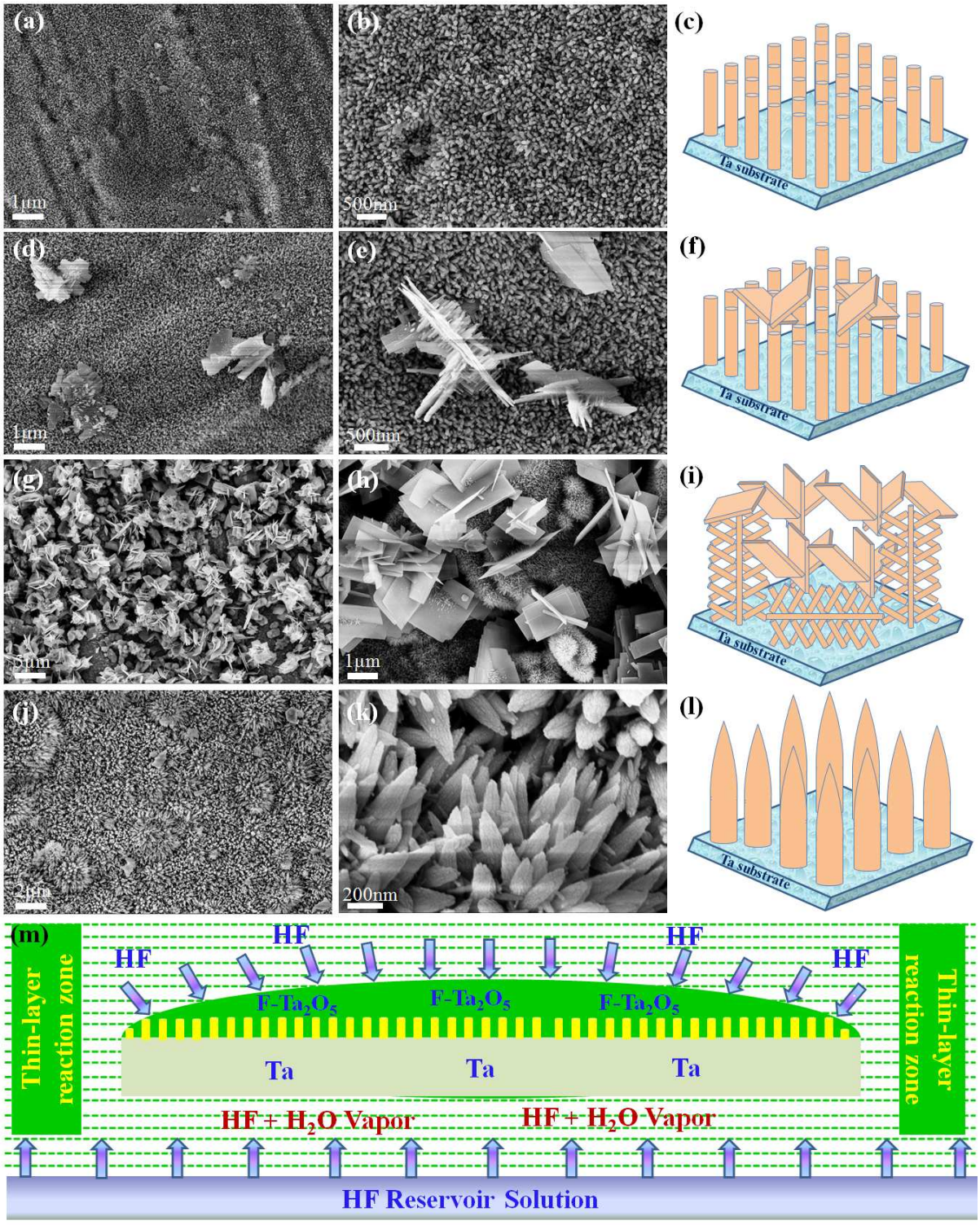

Figure 2. SEM images and schematic illustrations of (adgj) F-Ta_2O_5 and (behk) TaON arrays and (cfil) relative schematic illustration by vapor-phase hydrothermal process with increasing concentration of HF solution (M1 < M2 < M3 < M4). (abc), M1; (def), M2; (ghi), M3; (jkl), M4; and (m) schematic illustration of the proposed growth mechanism for nanostructures.

Based on the above experimental evidence, such distinctive nanostructures can be ascribed to the unique reaction environmental created under the hydrofluoric acid vapor-phase hydrothermal conditions. The tantalum species from the dissolution of the tantalum substrate diffuse into the HF solution and the structure formation can occur only after the concentration of the dissolved tantalum species in the reaction medium reaches saturation status. During this facile hydrothermal process, the mixed HF/H_2O solution concentration in the thin-layer reaction zone is determined by the dynamic equilibrium of the volatile reactant (e.g., HF) at the thin-layer reaction liquid/vapor/reservoir liquid interfaces. For this work, the direction of the dynamic equilibrium shift is driven by the consumption/release of HF in the thin-layer reaction zone (Figure 2m). Thus, after controlling the appropriate concentration of HF solution that eventually reaches a critical point with the efficient HF vapor pressure among the optimal thin-liquid-layer reaction zone, the large-scale shape-dependent TaON array were obtained on the Ta substrate by the gaseous mixture of HF and H_2O.

Interestingly, the intact geometric feature of TaON and Ba-TaON architectures were safely preserved even after the nitridation treatment; for instance, the Ba-TaON with hierarchinal structures did not collapse into generate numerous cracks. As shown in Figure 3a, the surface SEM images present the uniform distribution of the 1D/2D nanorod/nanosheet-assembled Ba-TaON architectures, demonstrating that there is no apparent variety upon the morphology after the barium-doped TaON. For Ba-TaON array, the 1D/2D nanorod/nanosheet-assembled architectures with an open and porous microstructure, are interconnected, improving the contact between the heterostructure surface and the electrolyte, which may be beneficial to transport the photogenerated charges between nanosheet and nanorod. After the deposition of C_3N_4 nanosheets and CoO_x nanoparticles, the C_3N_4 nanosheets are compactly distributed in the surface of the Ba-TaON

heterostructured array without obvious aggregation and the overall alignment of the Ba-TaON array is retained, as shown in Figure 3b. No significant changes in morphology were observed except a slight contrast enhancement by the loading of the CoO_x nanoparticles in C_3N_4/Ba-TaON array. Moreover, the combination analysis of X-ray photoelectron spectra (XPS) and energy dispersive X-ray spectra (EDS) of TaON, C_3N_4/Ba-TaON and CoO_x/C_3N_4/Ba-TaON heterojunction array indicate that the sample was consisted of the Co, C, N, O, Ba, and Ta elements, resulting into the formation of the CoO_x/C_3N_4/Ba-TaON heterojunction array (Figure S8-S11). Furthermore, the fine structures of these architectures were displayed from the relative TEM images in Figure 3(c-f). As shown in Figure 3c, the nanosheets possess well-defined tetragonal shapes with landscape dimension of 1~3 μm and the diameter of the nanorods is about 40~60 nm. In Figure 3d, the lattice spacings of 0.482 nm and 0.51 nm are observed, in good agreement with the (100) direction of 1D nanorod and the (200) direction of 2D nanosheet, respectively.[29-36] In Figure 4e, the C_3N_4 nanosheets and CoO_x nanoparticles intimately coat the surface of the hierarchical Ba-TaON architecture. Especially, it can be seen that the layered C_3N_4 naosheets cover the Ba-TaON array. Furthermore, as shown in Figure 4f, the lattice spacings of 0.25 nm and 0.46 nm have been indexed to the (111) crystal faces of CoO and Co_3O_4 nanoparticles,[39] indicating that the CoO_x nanoparticles consisting of CoO and Co_3O_4 nanoparticles, are homogeneously dispersed on the surface of C_3N_4/Ba-TaON.

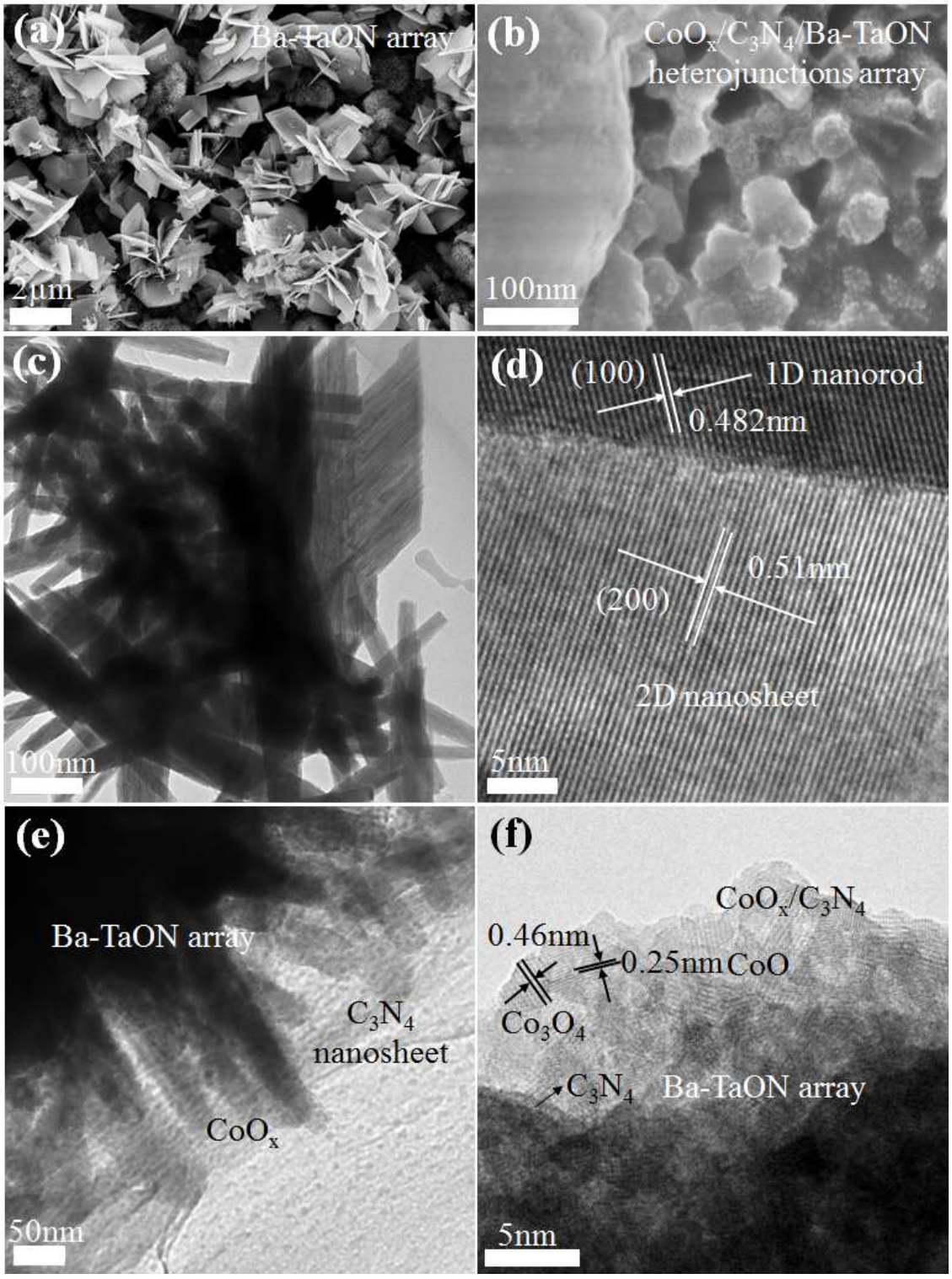

Figure 3. SEM (ab) and TEM (cdef) images of (acd) Ba-TaON and (cdef) hierarchical CoO_x/C_3N_4/Ba-TaON array.

In order to ascertain the crystal structure of the Ba-TaON and CoO_x/C_3N_4/Ba-TaON array, XRD

patterns and XPS spectra of the various samples have been conducted (Figure S12 and Figure 4). After Ba^{2+} doping, the analysis of XPS and XRD patterns indicates both TaON and Ba-TaON have the same crystal structure (Figure S8~S13), which is in good agreement with the phenomenon of barium-doped Ta_3N_5.[41] Moreover, the relative Co 2p, C 1s and N 1s peaks of CoO_x/C_3N_4/Ba-TaON array were conducted, as shown in Figure 4. Obviously, the two distinct peaks at 796.5 (Co $2p_{1/2}$) and 780.6 eV (Co $2p_{3/2}$) with a satellite peak at 787.1 eV are observed in the high-resolution Co 2p spectra, which is in good agreement with the positions of both the Co^{3+} and Co^{2+}.[20,39] The atomic percentage of Co on the surface of the CoO_x/C_3N_4/Ba-TaON array was estimated to be 2.5wt% based on XPS analysis. However, it was not detected upon the Ba-TaON and C_3N_4/Ba-TaON array for Co 2p XPS spectra. The C 1s peak can be deconvoluted into two peaks at ~285.1 and ~288.2 eV. The appearance of the C 1s peak at 288.2 eV indeed indicate that the C_3N_4 structure has changed after interaction with Ba-TaON to form the heterojunction, confirming the existence of chemical bonds between C_3N_4 and Ba-TaON in the heterojunctions, which is in agreement with the previous reports.[42-43] The N 1s XPS spectrafor the CoO_x/C_3N_4/ Ba-TaON array shows an asymmetrical feature indicating the coexistence of a number of nitrogen environments; fitting with three Gaussians results in binding energies of 398.8, 399.9, and 401.4 eV, which can be assigned to tertiary nitrogen ($N-(C)_3$) and amino functional groups having a hydrogen atom (C−N−H) as well as N atoms sp^2-bonded to two carbon atoms (C=N−C), thus confirming the presence of graphitic carbon nitride. To further convince this point, the Raman spectra of Ba-TaON and CoO_x/C_3N_4/Ba-TaON array has been conducted and it is clear to confirm the presence of carbon nitride (Figure S14). Thus, the analysis of the XRD patterns, XPS and Raman spectra indicates the formation of Ba-TaON, C_3N_4/Ba-TaON and CoO_x/C_3N_4/Ba-TaON heterostructured array.

Moreover, in order to examine the optical properties of as-prepared tantalum-based photoanodes,

the UV−vis DRS spectra of the different Ba-TaON, C_3N_4/Ba-TaON and CoO_x/C_3N_4/Ba-TaON heterojunction array are shown in Figure 4d. The UV−vis absorption of Ba-TaON semiconductor with the indirect band gap of 2.4 eV, has a clear edge around 500-600 nm, which is in good agreement with the previous report.[36,45] After the coupling the C_3N_4 nanosheets and CoO_x nanoparticles on the surface of Ba-TaON array, the UV−vis absorption of the CoO_x/C_3N_4/Ba-TaON heterostructured array shows the enhanced light scattering in the visible-light region.

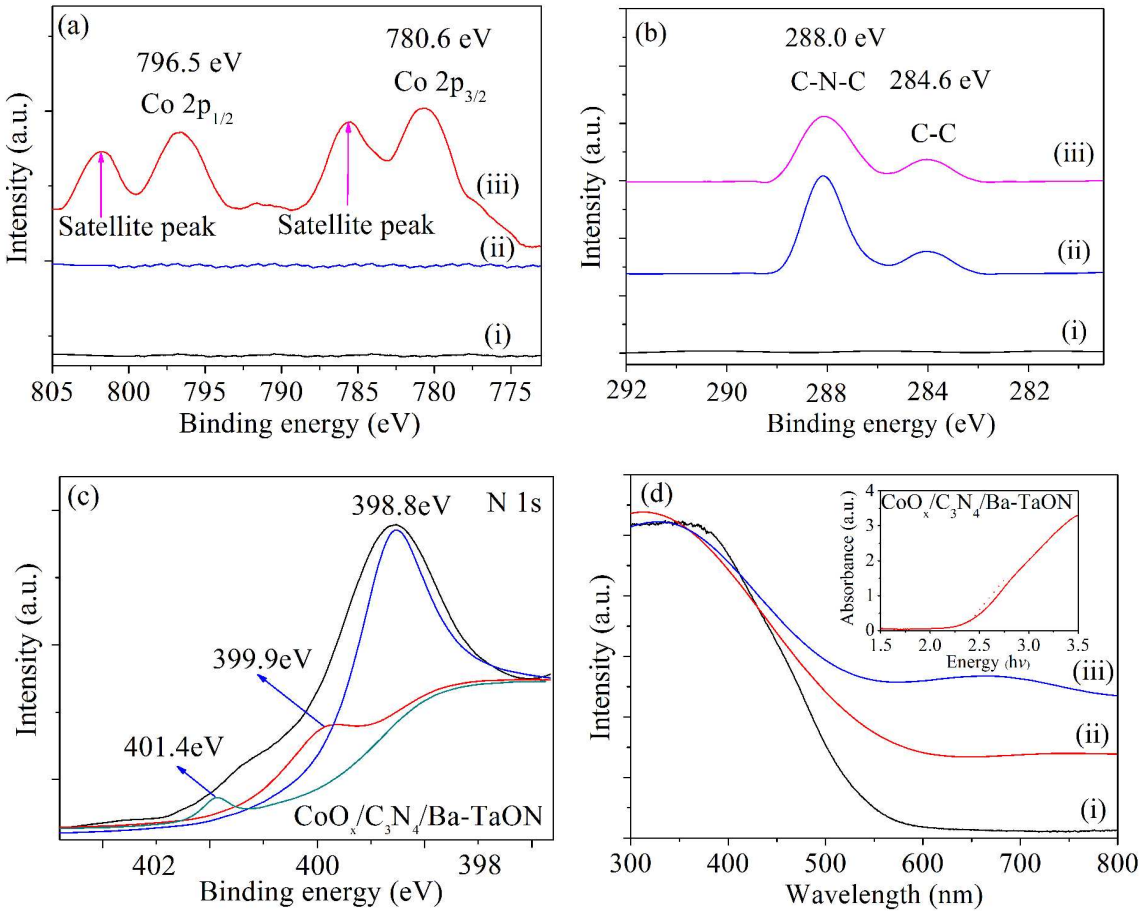

Figure 4. (a) Co 2p, (b) C 1s and (c) N 1s XPS spectra, and (d) UV−vis diffuse reflectance spectra of (i) Ba-TaON, (ii) C_3N_4/Ba-TaON and (iii) CoO_x/C_3N_4/Ba-TaON.

3.2 PEC water splitting of tantalum-based photoanodes

To quantify the activity of the arrays towards water splitting, the PEC performance of the

hierarchical TaON photoanode was conducted in NaOH electrolyte under AM 1.5G 100 mW/cm^2 simulated sunlight. Under the tunable nitridation temperature between 650 and 750 ^{o}C, the appropriate nitridation temperature for the TaON array is around 700 ^{o}C (Figure S15). As shown in Figure 5a, it is obvious that the photocurrent of three-dimensional architectured TaON array is higher than that of 1D nanorod array. After the introduction of barium doping, the Ba-TaON array presents the higher photocurrent than that of TaON array due to the enhanced electrical property (Figure S16/S17). Thus, it is confirmed that the nitridation temperature and the fabrication process play the pivot roles on the formation of TaON photoanode with high PEC performance. Currently, the utilization of graphitic carbon nitride (C_3N_4) semiconductor has emerged as a metal-free polymeric photocatalyst for various relevant applications.[46] Herein, C_3N_4 nanosheets were introduced into the Ba-TaON photoanode system for the construction of the C_3N_4/Ba-TaON heterojunction photoanode. Under AM 1.5G solar light, the photocurrent density of the C_3N_4/Ba-TaON heterojunction photoelectrode with 2.44 mA/cm^2 at 1.23 V vs. V_{RHE}, is much higher than that of TaON photoelectrode. However, the bare hierarchical Ba-TaON photoanode reached the photocurrent density of 1.15 mA/cm^2 at 1.23 V vs. RHE due to the serious recombination and photocorrosion.

In order to address the above-mentioned problem, the utilization of cobalt based catalyst modified the semiconductor for interfacial charge transfer, have been extensively investigated for PEC water splitting applications.[39] The CoO_x co-catalysts were employed for the decoration of the hierarchical C_3N_4/Ba-TaON photoanode. As shown in Figure 5b, the photocurrent density of the hierarchical CoO_x/C_3N_4/Ba-TaON heterojunction photoelectrode is much higher than that of Ba-TaON and C_3N_4/Ba-TaON photoelectrode under AM 1.5G solar light. Especially, the CoO_x/C_3N_4/Ba-TaON photoanode yielded a photocurrent density of 4.57 mA/cm^2 at 1.23 V vs.

RHE, which was ~1.9 and ~4.0 times higher than that of Ba-TaON and C_3N_4/Ba-TaON photoanode, exhibiting that not only the onset potential is negatively shifted but also the photocurrent is significantly improved due to the effective charge transfer process. In the potential range of 0.8~1.6 V vs. RHE, the photocurrent density in the CoO_x/C_3N_4/Ba-TaON photoanode is 1.5~5.4 mA/cm^2, indicating a significant transfer of the photogenerated holes in the PEC water splitting compared with the bare TaON array.

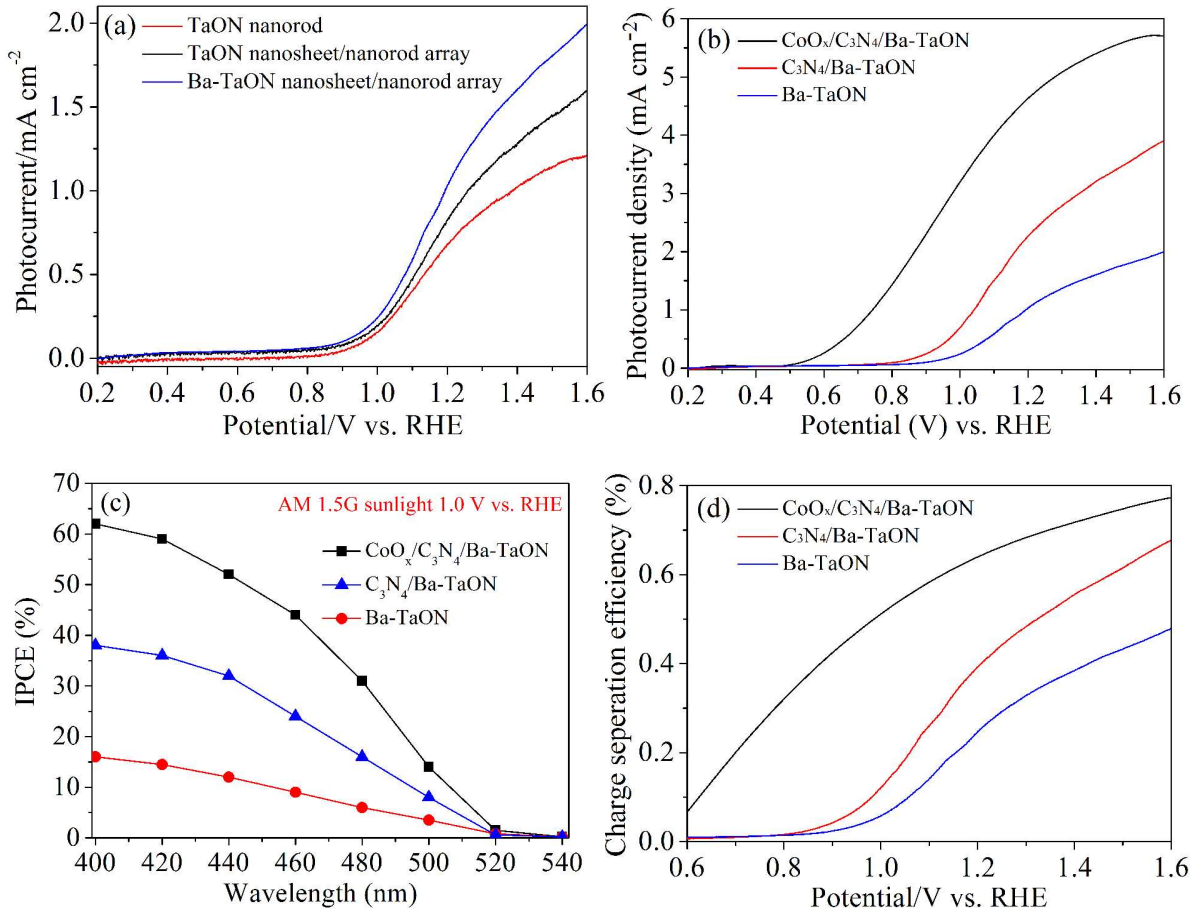

Figure 5. (ab) Photocurrent–potential curves, (c) IPCEs curves and (d) charge separation efficiency-potential curves under AM 1.5G-simulated sunlight of TaON NR array and 1D/2D nanorod/nanosheet-assembled TaON and Ba-TaON, C_3N_4/Ba-TaON and CoO_x/C_3N_4/Ba-TaON array under AM 1.5G irradiation.

Furthermore, the incident photon-to-electron conversion efficiencies (IPCEs) of the Ba-TaON, C_3N_4/Ba-TaON and CoO_x/C_3N_4/Ba-TaON photoanodes, have been conducted (Figure 5c). At 1.0 V vs. RHE, the IPCEs for the CoO_x/C_3N_4/Ba-TaON photoelectrode were above 50% in the range of 400~440 nm, which is higher than that of CoO_x/TaON electrode (*ca.* 42% at 400 nm at 1.2 V vs RHE in sodium phosphate).[13] It is worth to pointing out that a maximum IPCE of 62% was achieved at 400 nm for the CoO_x/C_3N_4/Ba-TaON array. Besides, the transient photocurrents also exhibit good switching behaviour at 1.23 V vs. RHE (Figure S18). All above-mentioned results demonstrate that the recombination of photoexcited carriers and photocorrosion of TaON photoanode are effectively inhibited through the modification of C_3N_4 and CoO_x.

To convince the recombination and separation of the photogenerated charges for the quantitative analysis, we examined the charge separation efficiencies of the Ba-TaON, C_3N_4/Ba-TaON and CoO_x/C_3N_4/Ba-TaON array by comparing the photocurrent from water and H_2O_2 oxidation (Figure S19/S20) while the H_2O_2, as a hole scavenger, was used for essessing the performance of surface hole injection.[40,47] Figure 5d shows that the charge separation efficiency of Ba-TaON photoanode is rather poor, indicating that the photogenerated holes are initially accumulated on the surface. After the deposition of C_3N_4 and CoO_x layers, the charge separation efficiencies of Ba-TaON photoanode is significantly enhanced, reaching 42% and 66% at a potential of 1.23 V vs. RHE, demonstrating that the heterojunction of C_3N_4/Ba-TaON photoanode is favorable to separate the photogenerated charges and the CoO_x acts as an efficient WOC that substantially promotes surface holes for water oxidation.

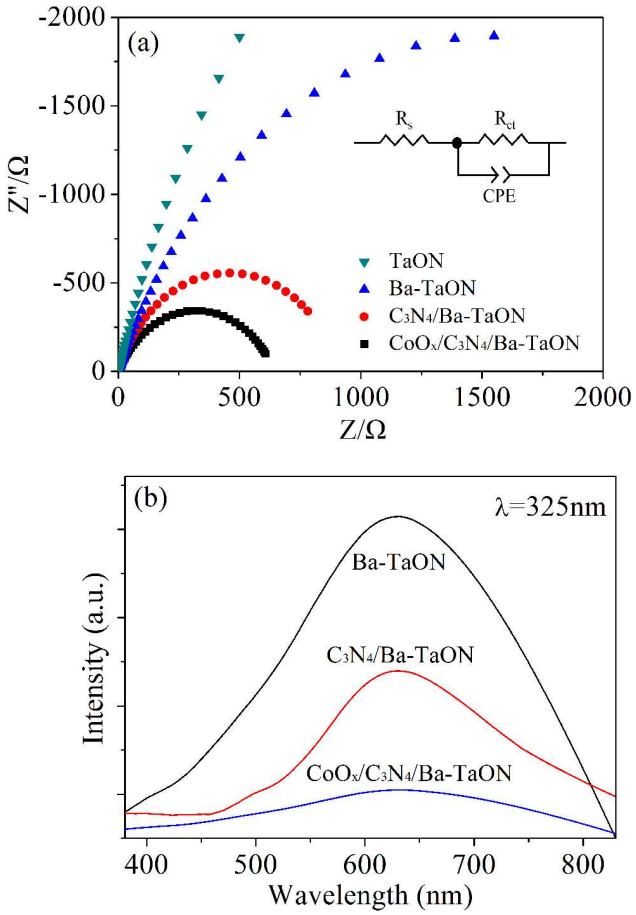

Figure 6. Nyquist plot measured at an applied potential of 1.0 V vs. RHE under AM 1.5G simulated sunlight and (b) photoluminescence spectra of the hierarchical TaON, Ba-TaON, C_3N_4/Ba-TaON and CoO_x/C_3N_4/Ba-TaON array excited at the wavelength of 325 nm.

To gain more insight into the principle of the enhancement of PEC performance, the analysis of electrochemical impedance spectroscopy (EIS) for different samples were conducted in Figure 6a. It is obvious that the arch for the Ba-TaON arrays was much smaller than that of TaON due to the large impedance of TaON electrode. The smallest arch of the CoO_x/C_3N_4/Ba-TaON array indicate that the decoration of the C_3N_4 nanosheets and CoO_x nanoparticles significantly reduced the resistance on the movement of charge carriers due to the fast transport of charge carriers. Moreover, the photoluminescence (PL) spectra of the Ba-TaON, C_3N_4/Ba-TaON and CoO_x/C_3N_4/Ba-TaON

arrays are shown in Figure 6b. The excitation wavelength is determined as 325 nm, and the pristine Ba-TaON has a strong emission peak at about 630 nm. The lowest PL peak of the CoO_x/C_3N_4/Ba-TaON array demonstrates that the recombination of photoexcited carriers is effectively inhibited through the modification of C_3N_4 and CoO_x, which can accelerate the water splitting reaction and improve the charge transfer processes.

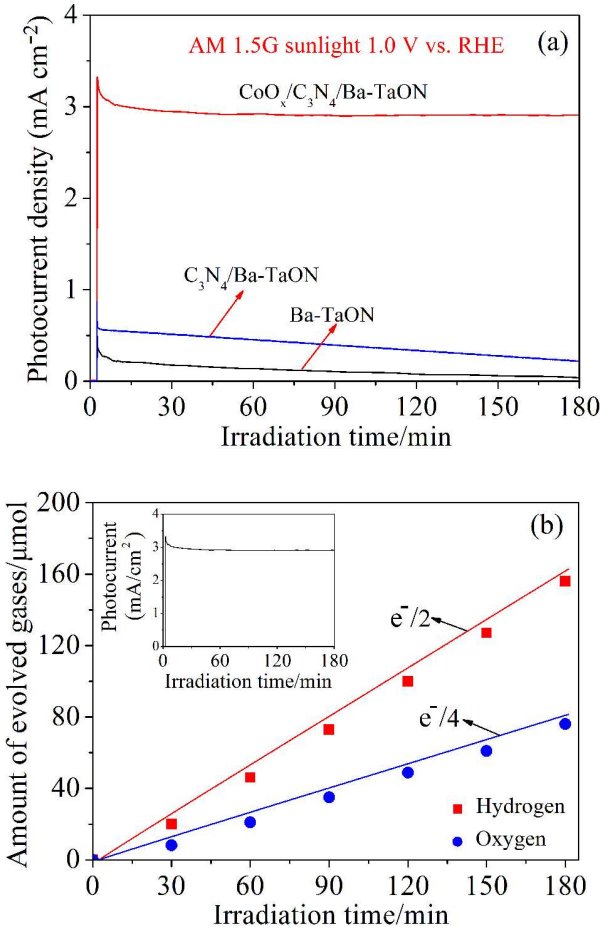

Figure 7. (a) Time courses for hierarchical Ba-TaON, C_3N_4/Ba-TaON and CoO_x/C_3N_4/Ba-TaON photoanodes at 1.0 V vs. RHE, (b) H_2 and O_2 evolution for the CoO_x/C_3N_4/Ba-TaON photoanode at 1.0 V vs. RHE under AM 1.5G irradiation. The expected amount of hydrogen molecules, $e^-/2$, is presented in a solid line. The inset shows the time course of photocurrent generation.

After the enhancement of photocurrent through the TaON array, the major aim of this work is

also to improve the photostability of TaON photoanode. Herein, the effect of CoO_x and C_3N_4 on the photostability of Ba-TaON array was examined. As shown in Figure 7a, the photocurrent of the Ba-TaON array decreases significantly within a short times, indicating that accumulation of photogenerated holes at the surface of Ba-TaON. Noticeably, the high photocurrent of ~3.01 mA/cm^2 for CoO_x/C_3N_4/Ba-TaON photoanodes remains after 180 min irradiation, indicating that the decoration of CoO_x and C_3N_4 efficiently improve the transport of photogenerated charge carriers.[16,17,41] Compared with that of IrO_x/TaON and CoO_x/TaON,[11,13] the CoO_x/C_3N_4/Ba-TaON photoanode has exhibited the significant enhancement of the stable water splitting. Furthermore, as shown in Figure 6b, the amounts of oxygen and hydrogen evolved from the 3D CoO_x/C_3N_4/Ba-TaON photoanode and the Pt counter electrode were 77.6 and 156.0 μmol cm^{-2}, respectively. The ratio of evolution rates of H_2 and O_2 is almost close to the stoichiometric value of 2.0. Faradaic efficiencies of 96% and 93%, respectively, are obtained as determined by measurement of the evolved H_2 and O_2 gas, indicating that the photocurrent is indeed due to the oxygen evolution reaction (OER) and hydrogen evolution reaction (HER).

Based on the above–mentioned results, a possible PEC water splitting mechanism is proposed for the hierarchical CoO_x/C_3N_4/Ba-TaON heterojunction photoanode. After the decoration of C_3N_4 nanosheets, as shown in Figure 8, the electrons from C_3N_4 move toward Ta substrate through Ba-TaON, and the holes from Ba-TaON migrate to surface of C_3N_4 according to the potential difference of C_3N_4 (E_g = 2.7 eV, E_{CB} = −1.13 and E_{VB} = +1.57 eV)[37] and Ba-TaON (E_g = 2.4 eV, E_{CB} = −0.3 and E_{VB} = +2.1 eV).[36] Thus, the C_3N_4/Ba-TaON heterojunction photoanode can improve the efficient charge separation across the junction structure for the PEC water splitting performance. To further improve the photocurrent and photostability of C_3N_4/Ba-TaON photoanodes, the CoO_x nanoparticles in the CoO_x/C_3N_4/Ba-TaON photoanode behave as an electron conductor to enhance

the electron–hole separation and easily transfer the electrons from the conduction band of C_3N_4 to the conduction band of the Ba-TaON array and then flow to the Ta substrate along the Ba-TaON, providing a conductive electron transport "highway". The electrons ultimately transfer to the Pt counter electrode to reduce water. At the same time, the oxygen evolution was produced by the oxidation of water using the accumulated holes on the protective surface of the CoO_x nanoparticles from Co^{2+} to Co^{3+}/Co^{4+} and finally to Co^{4+}–O intermediates.[35,39,47] Therefore, the unique 3D CoO_x/C_3N_4/Ba-TaON heterojunction photoanode, is more favorable to the separation of photogenerated electron–hole pairs, which contributes to the high PEC performance and photostability for solar-driven water splitting.

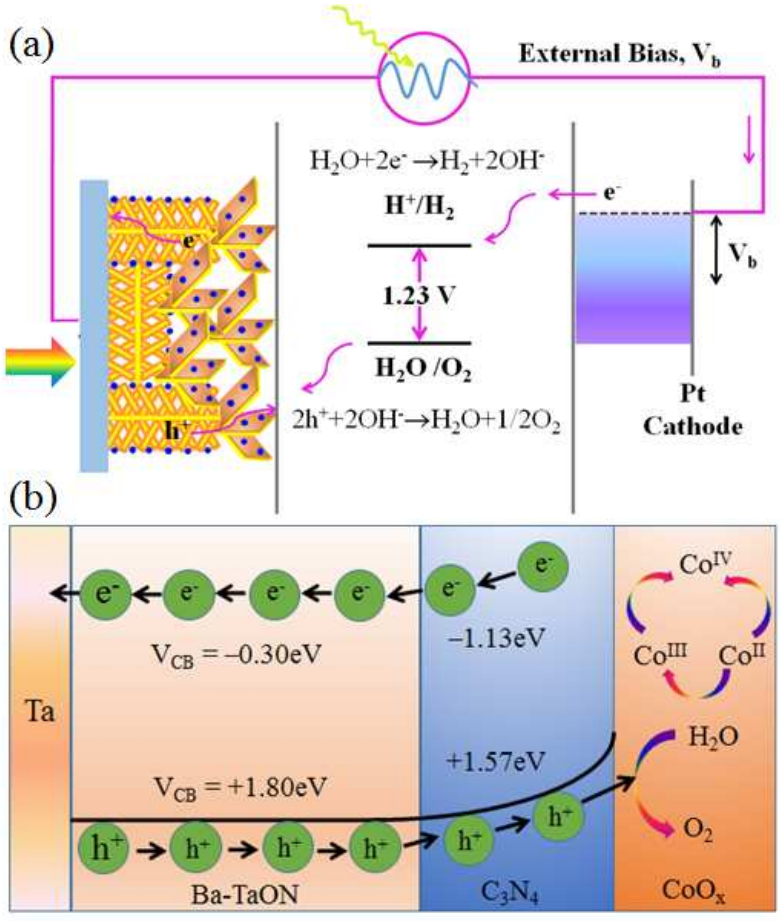

Figure 8. Schematic illustration for (a) the photoelectrochemical water splitting and (b) the transfer of charge carriers of the hierarchical CoO_x/C_3N_4/Ba-TaON heterojunction photoanode.

4. Conclusion.

In summary, three-dimensional CoO_x/C_3N_4/Ba-TaON heterojunction photoanode were fabricated for PEC solar water splitting. With the help of the controllable vapor-phase hydrothermal technique and subsequent nitridation, the dimensionality-dependent TaON photoanodes with 1D nanorod array, 1D/2D nanorod/nanosheet-assembled architectures and 1D spindle nanostructured array were fabricated. After the doping strategy, the 1D/2D nanorod/nanosheet-assembled Ba-TaON photoanode presented a high PEC activity. Especially, as a return for the innovative stack design, the integrated 3D heterojunction photoanodes comprising the 1D/2D nanorod/nanosheet-assembled Ba-TaON array and 2D C_3N_4 nanosheets decorated with CoO_x nanoparticles were successfully prepared and the 3D CoO_x/C_3N_4/Ba-TaON photoanodes with within expectation possessed the pronounced photocurrent of 4.57 mA/cm^2 at 1.23 V vs. RHE and the remarkable photostability under AM 1.5G simulated sunlight. This enhancement originates primarily from effective charge migration according to the analysis of PEC performance, the quantitative analysis combined with the electrochemical impedance and photoluminescence analysis. In this regard, the synergistic effects of nanoengineering from composition regulation, morphology innovation and heterojunction construction show great significance of designing highly efficient and dimensionality-dependent photoelectrodes for the application in solar conversion.

Acknowledgements

This work was supported by National Science Foundation of China (No. 51472027 and 51102015), Beijing High School Youth Talent Plan (YETP0351) and National Basic Research Program of China (973 Program, No. 2013CB632404). J. G. Hou thanks the Japan Society for the

Promotion of Science (JSPS) for a support in the form of a fellowship tenable at Tohoku University, Sendai, Japan.

Supporting Information Available: XRD pattern, EDX spectra, SEM and TEM images, and photocurrent measurements. This material is available free of charge via the Internet.

References

1. M. Grätzel, *Nature* **2001**, *414*, 338.
2. X. B. Chen, S. H. Shen, L. J. Guo, S. S. Mao, *Chem. Rev.* **2010**, *110*, 6503.
3. S. W. Boettcher, J. M. Spurgeon, M. C. Putnam, E. L. Warren, D. B. Turner-Evans, M. D. Kelzenberg, J. R. Maiolo, H. A. Atwater, N. S. Lewis, *Science* **2010**, *327*, 185.
4. A. Fujishima, K. Honda, *Nature* **1972**, *238*, 37.
5. S. J. Hong, S. Lee, J. S. Jang, J. S. Lee, *Energy Environ. Sci.* **2011**, *4*, 1781.
6. K. Sivula, F. Le Formal, M. Gratzel, *Chem. Sus. Chem.* **2011**, *4*, 432.
7. W. J. Luo, Z. S. Yang, Z. S. Li, J. Y. Zhang, J. G. Liu, Z. Y. Zhao, Z. Q. Wang, S. C. Yan, T. Yu, Z. G. Zou, *Energy Environ. Sci.* **2011**, *4*, 4046.
8. K. Iwashina, A. Kudo, *J. Am. Chem. Soc.* **2011**, *133*, 13272.
9. K. Maeda, K. Domen, *J. Phys. Chem. C* **2007**, *111*, 7851.
10. M. Higashi, K. Domen, R. Abe, *Energy Environ. Sci.* **2011**, *4*, 4138.
11. Z. Wang, J. G. Hou, C. Yang, S. Q. Jiao, K. Huang, H. M. Zhu. *Energy Environ. Sci.* **2013**, *6*, 2134.
12. M. Higashi, K. Domen, R. Abe, *J. Am. Chem. Soc.***2012,** *134*, 6968.
13. R. Abe, M. Higashi, K. Domen, *J. Am. Chem. Soc.* **2010**, *132*, 11828.

14. K. Maeda, M. Higashi, D. L. Lu, R. Abe, K. Domen, *J. Am. Chem. Soc.* **2010**, *132*, 5858.

15. M. J. Liao , J. Y. Feng , W. J. Luo , Z. Q. Wang , J. Y. Zhang , Z. S. Li , T. Yu , Z. G. Zou, *Adv. Funct. Mater.* **2012**, *22*, 3066.

16. M. X. Li, W. J. Luo, D. P. Cao, X. Zhao, Z. S. Li, T. Yu, Z. G. Zou, *Angew. Chem. Int. Ed.* **2013**, *52*, 1.

17. C. Zhen, L. Z. Wang, G. Liu, G. Q. Lub, H. M. Cheng, *Chem. Commun.* **2013**, *49*, 3019.

18. J. G. Hou, Z. Wang, C. Yang, S. Q. Jiao, H. M. Zhu. *Energy Environ. Sci.* **2013**, *6*, 3322.

19. K. Maeda, M. Higashi, B. Siritanaratkul, R. Abe, K. Domen, *J. Am. Chem. Soc.* **2011**, *133*, 12334.

20. a) M. Matsukawa, R. Ishikawa, T. Hisatomi, Y. Moriya, N. Shibata, J. Kubota, Y. Ikuhara, K. Domen, Nano Lett. 2014, 14, 1038; b) F. X. Zhang, A. Yamakata, K. Maeda, Y. Moriya, T. Takata, J. Kubota, K. Teshima, S. Oishi, K. Domen, *J. Am. Chem. Soc.* **2012**, *134*, 8348.

21. H. Gao, C. Liu, H. E. Jeong, P. Yang, *ACS Nano* **2012**, *6*, 234.

22. a) I. Cesar, A. Kay, J. A. G. Martinez, M. Grätzel, *J. Am. Chem. Soc.* **2006**, *128*, 4582; b) A. Kay, I. Cesar, M. Grätzel, *J. Am. Chem. Soc.* **2006**, *128*, 15714; c) Y. Hou, F. Zuo, A. Dagg, P. Y. Feng, *Angew. Chem. Int. Edit.* **2013**, *52*, 1248

23. C. Weisbuch, B. Vinter, Quantum Semiconductor Structures: Fundamentals and Applications; Academic Press: San Diego, CA, 1991.

24. D. Wang, F. Qian, C. Yang, Z. H. Zhong, C. M. Lieber, *Nano Lett.* **2004**, *4*, 871.

25. B. O. Dabbousi, J. RodriguezViejo, F. V. Mikulec, J. R. Heine, H. Mattoussi, R. Ober, K. F. Jensen, M. G. Bawendi, *J. Phys. Chem. B* **1997**, *101*, 9463.

26. C. Li, Y. F. Yu, M. F. Chi, L. Y. Cao, *Nano Lett.* **2013**, *13*, 948.

27. J. Shi, Y. Hara, C. L. Sun, M. A. Anderson, X. D. Wang, *Nano Lett.* **2011**, *11*, 3413.

28. S. W. Boettcher, J. M. Spurgeon, M. C. Putnam, E. L. Warren, D. B. Turner-Evans, M. D. Kelzenberg, J. R. Maiolo, H. A. Atwater, N. S. Lewis, *Science* **2010**, *327*, 185.

29. X. Feng, T. J. LaTempa, J. I. Basham, G. K. Mor, O. K. Varghese, C. A. Grimes, *Nano Lett.* **2010**, *10*, 948.

30. S. Banerjee, S. K. Mohapatra, M. Misra, *Chem. Commun.* **2009**, 7137.

31. Y. B. Li, T. Takata, D. Cha, K. Takanabe, T. Minegishi, J. Kubota, K. Domen, *Adv. Mater.* **2013**, *25*, 125.

32. J. G. Hou, Z. Wang, W. Kan, S. Q. Jiao, H. M. Zhu and R. V. Kumar, *J. Mater. Chem.*, **2012**, 22, 7291–7299.

33. J. G. Hou, C. Yang, Z. Wang, Q. Ji, Y. Li, G. Huang, S. Q. Jiao, H. M. Zhu, *Appl. Catal. B*, **2013**, *142–143*, 579–589.

34. S. C. Yan, S. B. Lv, Z. S. Li, Z. G. Zou, *Dalton Trans.*, **2010**, *39*, 1488–1491.

35. E. S. Kim, N. Nishimura, G. Magesh, J. Y. Kim, J. W. Jang, H. Jun, J. Kubota, K. Domen, and J. S. Lee, *J. Am. Chem. Soc.*, **2013**, *135*, 5375−5383.

36. J. G. Hou, C. Yang, H. J. Cheng, S. Q. Jiao, O. Takeda and H. M. Zhu, *Energy Environ. Sci.*, **2014**, **7**, 3758−3768.

37. G. P. Dong, Y. H. Zhang, Q. W. Pan, J. R. Qiu, *J. Photoch. Photobio. C*, **2014**, *20*, 33–50.

38. F. Yang, V. Kuznietsov, M. Lublow, C. Merschjann, A. Steigert, J.Klaer, A. Thomase, T. Schedel-Niedrig, *J. Mater. Chem. A*, **2013**, 1, 6407–6415.

39. Y. Hou, F. Zuo, A. P. Dagg, J. Liu, P. Y. Feng, *Adv. Mater.*, **2014**, *26*, 5043–5049.

40. M. Zhou, J. Bao, W. T. Bi, Y. Q. Zeng, R. Zhu, M. S. Tao, Y. Xie, *ChemSusChem* **2012**, *5*, 1420.

41. Y. Li, L. Zhang, A. Torres-Pardo, J. M. González-Calbet, Y. Ma, P. Oleynikov, O. Terasak, S. Asahina, M. Shima, D. Cha, L. Zhao, K. Takanabe, J. Kubota, K. Domen, *Nat. Comm.*, **2013**, *4*,

2566.

42. S. C. Yan, Z. S. Li, Z. G. Zou, *Langmuir*, **2009**, *25*, 10397.

43. L. Sun, X. Zhao, C. J. Jia, Y. Zhou, X. Cheng, P. Li, L. Liu, W. Fan, *J. Mater. Chem.*, **2012**, 22, 23428.

44. Q. J. Xiang, J. G. Yu, M. Jaroniec, *J. Phys. Chem. C*, **2011**, *115*, 7355−7363.

45. A. Suzuki, Y. Hirose, D. Oka, S. Nakao, T. Fukumura, S. Ishii, K. Sasa, H. Matsuzaki, T. Hasegawa, *Chem. Mater.,* **2014**, *26*, 976−981.

46. (a) X. Wang, K. Maeda, A. Thomas, K. Takanabe, G. Xin, J. M. Carlsson, K. Domen, M. Antonietti, *Nat. Mater.*, **2009**, *8*, 76−80; (b) K. Maeda, K. Sekizawa, O. Ishitani, *Chem. Commun.*, **2013**, *49*, 10127−10129; (c) X. Ye, Y. Cui, X. Wang, *ChemSusChem*, **2014**, *7*, 738−742; (d) Y. Chen, J. Zhang, M. Zhang, X. Wang, *Chem. Sci.*, **2013**, *4*, 3244−3248.

47. D. K. Zhong, S. Choi, D. R. Gamelin, *J. Am. Chem. Soc.*, **2011**, 133, 18370.

Broader context

With the increasing interest in solar energy utilization for energy crises, solar-driven water splitting is one of the promising approach that can mimic artificial photosynthesis to directly harvest and convert solar energy into clean and sustainable hydrogen energy. Tantalum oxynitride (TaON) semiconductors are potential candidates of photoanode materials for solar water splitting. However, the effective harvesting of solar energy and suppression of charge carrier recombination, which have unique dimensionality-dependent integrative and synergic effects are intriguing but still underdeveloped. Herein, we have designed and fabricated 2D carbon nitride nanosheets coupled 1D/2D nanorod/nanosheet-assembled barium-doped TaON array decorated with CoO_x nanoparticles as integrated 3D heterojunction photoanodes, exhibiting that not only the onset potential is negatively shifted but also the photocurrent and photostability are significantly improved. The rapid charge transport of the unique hierarchical structure, and the matched energy levels of C_3N_4, Ba-TaON and CoO_x efficiently boost the photogenerated charge carriers separation and transfer across the interfacial domain of hierarchical heterojunction. To help guide continuing research in this field, we identify key challenges that must be overcome to drive down the possible application of oxynitride photoanodes for PEC water splitting.

Graphical Abstract

The hierarchically CoO_x decorated 2D C_3N_4 nanosheets-3D nanorod/nanosheet-assembled barium-doped Ta_3N_5 heterojunction photoanode exhibited the the enhanced photocurrent density and durable photostability for photoelectrochemical solar water splitting.